

# Numerical Study of DC Argon Arc with Axial Magnetic Fields

Tang Chen · Zhang Xiaoning · Bing Bai ·  
Zimu Xu · Cheng Wang · Weidong Xia

Received: 15 March 2014 / Accepted: 8 October 2014 / Published online: 3 December 2014  
© Springer Science+Business Media New York 2014

**Abstract** Numerical simulation of an atmospheric DC arc under an axial magnetic field (AMF) is performed with a model of unifying the plasma and electrodes. In the model the configuration of the cathodic arc attachment is free. Results are given for a 200A argon arc under 0–0.02T AMF. The simulation results indicate that, with the AMF, the cathode arc attachment shrinks towards its tip. That induces many changes of arc configuration and arc parameters, different from the calculation assuming a fixed cathodic arc attachment: as the AMF increases, the plasma temperature nearby the cathode tip increases higher; the low temperature hollow of plasma nearby the anode expands more intensively in both axial and radial direction; the profile of current density on the anode exhibits a bigger concave shape; arc voltage drop increases more; and more power is delivered to the anode. The elements that cause the changes are discussed.

**Keywords** Axial magnetic field · Cathodic arc attachment · MHD pumping · Cathode jet

## Introduction

DC arc between a pointed rod cathode and a plate anode, which is called free burning arc, with currents in the range 10–10<sup>4</sup> A, is widely used in different kinds of manufacturing processes, such as welding, material surface processing, metallurgy [1, 2] and etc. Extensive numerical

---

T. Chen · Z. Xiaoning · B. Bai · Z. Xu · C. Wang · W. Xia (✉)  
Department of Thermal Science and Energy Engineering, University of Science and Technology  
of China, Hefei 230027, China  
e-mail: xiawd@ustc.edu.cn

T. Chen  
e-mail: chentang@mail.ustc.edu.cn

B. Bai  
Full Dimension Power Tech. Co., Ltd, D Block 6th Floor of Gem Techcenter, No. 9 Shangdi 3rd Street,  
Haidian District, Beijing 100085, China

studies on DC arc plasma have been conducted to predict arc properties as well as electrodes properties [3–12]. For practical application, an external magnetic field is usually imposed on free burning arc in order to change the arc configuration [13]. In some cases an external magnetic field may be applied on purpose to control the plasma deflection for a better welding quality [14]. In other situations, axial magnetic field (AMF) is used to restrict arc developing radially, so as to increase arc intensity as well as energy flux to the anode. Based on this effect, imposed AMF is used to focus arc lamp column [15]. With 0.02T AMF on xenon lamp, the radiation power of arc column dramatically increases by 70 %, most of them coming from the area in front of cathode tip [16]. The radiation efficiency increases by 23 % [16]. For welding applications, the AMF would increase the arc voltage, the temperature amplitude of plasma and heat transfer to the anode [13]. With the AMF increasing, the arc column slightly shrinks nearby the cathode, and expands nearby the anode [17, 18].

In order to understand the AMF effect on the free arc, Li [19, 20] performed a 2D simulation using a model with fixed current density and temperature boundary conditions on cathode surface (following called as “Fixed Cathodic Arc Attachment” Model-FCAM). The results are shown in Fig. 1. With 0.02T AMF, the high temperature core of the arc plasma retracts towards the cathode significantly, so that the high temperature core expands radially; the arc presents a “hollow bell shape”, which is similar to the experimental results to some extent. Yin [21] has conducted a 3D numerical study on welding pool under the influences of applied axial magnetic fields. Quite similar to Li’s work [19], Yi’s 3D simulation also reveals that the rotating of the arc should induce a hollow region in front of anode. Ref. [22] indicated that AMF induces the arc rotating and the centrifugal flowing in near-anode region, which drags plasma off axis and causes low pressure nearby the anode. The arc retracts towards the cathode tip, compressing the plasma, so that the maximum temperature near the cathode tip increases [22].

So far the experimental and numerical researches on free arc under AMF only concerned for arc column and anode arc root, but not for a variation of the arc attachment on the cathode. A key fact is that, the shape of the cone cathode tip and the current density profile on it can strongly affect the cathode jet and hence the whole arc configuration. Previous experimental researches indicated that AMF rotating arc may vary arc’s attachment on the cathode [16, 23–25]. So numerical research on AMF effects should unify the arc column and the cathode. In this way the cathodic arc attachment behavior under AMF as well as the consequent influence on arc column can be studied.

A fine prediction of cathodic arc attachment requires a model on plasma-cathode interaction. In the community, models concerning plasma-cathode interaction can be divided into three categories [26].

The first one involves the interaction of cathode-plasma sheath region but decouples the plasma from the cathode sheath [27–32]. The heating flux to the cathode surface is usually described by a one-dimensional non-linear method [28] and is concerned with cathode surface temperature and current density. The arc column’s influence on cathodic arc attachment is neglected. By using the model [33], Benilov has predicted multi-cathodic arc roots and diffuse arc root. Employing the modeling results [28] \_ENREF\_33as the boundary conditions for plasma column, Li [11, 12] researched on the non-equilibrium characteristics of DC arc. Being decoupled from the plasma, the model is not proper for studying variations of the cathodic arc attachment affected by arc plasma behavior under AMF.

The second one assumes the current continuity between the cathode and the plasma but neglects the cathode layer [7, 34–36]. The model has to fix some arbitrary settings (for example, 3,500 K) as insulation limit on the cathode surface [7]. In other words, this kind of model is not physically self-consistent and only gives a rough prediction of cathodic arc attachment.

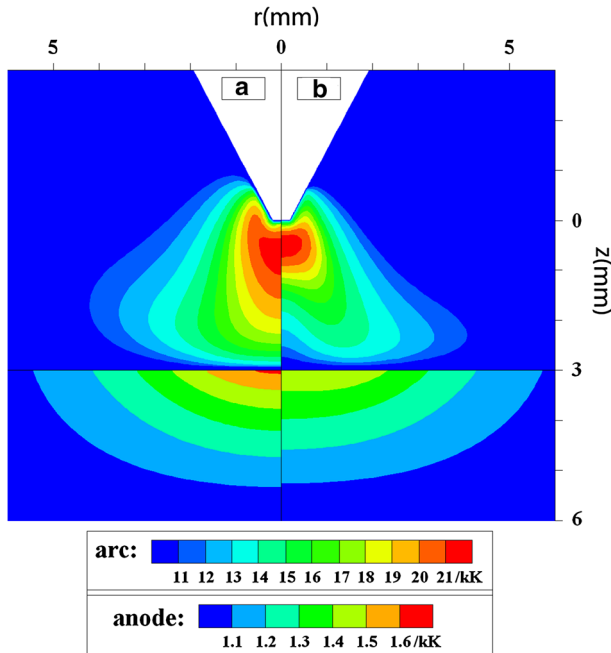


**Fig. 1** Temperature contour [1] with (a) 0T and (b) 0.02T AMF,  $I = 200A$ , arc gap 3 mm

The third one takes into account the cathode, the LTE arc column and the pre-sheath region [3, 4, 37–39], so that the interaction between arc cathodic attachment and arc plasma could be reflected. The modelling takes into account the ambipolar diffusion of ions in presheath but neglects the whole sheath layer [4]. By doing so, one can ensure the continuity of current density from plasma to cathode. The model [4, 40–42] has been compared with experimental data and the calculated cathode temperatures are in reasonable agreement with experimental results. Since the current density on the cathode surface is highly related to cathode surface temperature and a large proportion of it is electron thermionic part, one can infer that the calculated current density can be believable. Recently, by applying J. J. Lowke’s method [4], B Bai has focused on the simulation of magnetically dispersed arc [23, 43].

Concerning for the variation of the cathodic arc attachment, we select a simple LTE model of unifying electrodes and plasma (which was presented by Lowke et al. [4], following called as “Variable Cathodic Arc Attachment” Model-VCAM), to study the arc discharge under AMF. D\_ENREF\_5etails of this model can be found in references [3, 4, 39]. The AMF induced variations of the configuration of the arc column as well as the cathodic and anodic arc attachments are present and analyzed. The differentials between results from VCAM and FCAM are also given.

## Numerical Model

### ARC Column Model

In this study of high intensity argon arc at atmospheric pressure with arc current about 200A, local thermodynamic equilibrium (LTE) state is a reasonable approximation for the arc column

region [44]. Experimental results show that the rotating plasma under AMF is homogeneous in tangential direction [45], which means axisymmetric assumption is appropriate. The simulation is based on the following assumptions: (a) the plasma flow is swirling, axisymmetric, steady, and turbulent; (b) plasma is in the LTE state and optically thin to radiation; (c) motional electric field is neglected, but Lorentz force generated by self-induced magnetic field's is taken into account; (d) the work of the pressure gradient and gravity effect is neglected. Based on those assumptions, the governing equations in cylindrical coordinates ( $z, r$ ) are as follows.

Mass conservation equation:

$$\frac{1}{r} \frac{\partial}{\partial r} (r \rho v_r) + \frac{\partial}{\partial z} (\rho v_z) = 0 \quad (1)$$

Momentum conservation equations:

$$\frac{1}{r} \frac{\partial}{\partial r} (r \rho v_r^2) + \frac{\partial}{\partial z} (\rho v_r v_z) = -\frac{\partial P}{\partial r} + \frac{1}{r} \frac{\partial}{\partial r} \left( 2r \Gamma_u \frac{\partial v_r}{\partial r} \right) + \frac{\partial}{\partial z} \left( \Gamma_u \frac{\partial v_r}{\partial z} + \Gamma_u \frac{\partial v_z}{\partial r} \right) - 2\Gamma_u \frac{v_r}{r^2} + F_r \quad (2)$$

$$\frac{1}{r} \frac{\partial}{\partial r} (r \rho v_r v_z) + \frac{\partial}{\partial z} (\rho v_z^2) = -\frac{\partial P}{\partial z} + \frac{\partial}{\partial z} \left( 2\Gamma_u \frac{\partial v_z}{\partial z} \right) + \frac{1}{r} \frac{\partial}{\partial r} \left( r \Gamma_u \frac{\partial v_r}{\partial z} + \Gamma_u \frac{\partial v_z}{\partial r} \right) + F_z \quad (3)$$

$$\frac{1}{r} \frac{\partial}{\partial r} (r \rho v_r v_\theta) + \frac{\partial}{\partial z} (\rho v_z v_\theta) = \frac{\partial}{\partial z} \left( \Gamma_u \frac{\partial v_\theta}{\partial z} \right) + \frac{1}{r} \frac{\partial}{\partial r} \Gamma_u \left( r \frac{\partial v_\theta}{\partial r} - v_\theta \right) + \frac{2}{r} \Gamma_u \left( \frac{\partial v_\theta}{\partial r} - \frac{v_\theta}{r} \right) - \rho \frac{v_r v_\theta}{r} + F_\theta \quad (4)$$

Energy conservation equation:

$$\frac{1}{r} \frac{\partial}{\partial r} (r \rho v_r h) + \frac{\partial}{\partial z} (\rho v_z h) = \frac{1}{r} \frac{\partial}{\partial r} \left( r \Gamma_T \frac{\partial T}{\partial r} \right) + \frac{\partial}{\partial z} \left( \Gamma_T \frac{\partial T}{\partial z} \right) + \frac{j_z^2 + j_r^2}{\sigma} + U + \frac{5k}{2e} \left( \frac{j_z}{C_p} \frac{\partial h}{\partial z} + \frac{j_r}{C_p} \frac{\partial h}{\partial r} \right) \quad (5)$$

Electric potential equation:

$$\frac{1}{r} \frac{\partial}{\partial r} \left( r \sigma \frac{\partial \varphi}{\partial r} \right) + \frac{\partial}{\partial z} \left( \sigma \frac{\partial \varphi}{\partial z} \right) = 0 \quad (6)$$

Magnetic potential equations:

$$\frac{1}{r} \frac{\partial}{\partial r} \left( r \sigma \frac{\partial A_z}{\partial r} \right) + \frac{\partial}{\partial z} \left( \sigma \frac{\partial A_z}{\partial z} \right) = -\mu_0 j_z \quad (7)$$

$$\frac{1}{r} \frac{\partial}{\partial r} \left( r \sigma \frac{\partial A_r}{\partial r} \right) + \frac{\partial}{\partial z} \left( \sigma \frac{\partial A_r}{\partial z} \right) = -\mu_0 j_r + \frac{A_r}{r^2} \quad (8)$$

$$B_\theta = \frac{\partial A_r}{\partial z} - \frac{\partial A_z}{\partial r} \quad (9)$$

Here  $v_r, v_z$  and  $v_\theta$  are the radial, axial and tangential component of mass average velocity  $\mathbf{v}$ .  $\rho, p, T, h$  are plasma density, pressure, MHD temperature, and enthalpy respectively.  $\mu, \kappa, \sigma, U$  are

temperature-dependent plasma properties (in laminar flow state) of viscosity, thermal conductivity, electric conductivity, radiation power per unit volume respectively.  $\Gamma_u$  and  $\Gamma_T$  are plasma viscosity and thermal conductivity in turbulent state.  $j_r$  and  $j_z$  are radial and axial current density  $\mathbf{j} = \sigma \mathbf{E}$ .  $B_\theta$  and  $B_z$  are self-induced and external axial component of magnetic field  $\mathbf{B}$ .  $F_\theta$ ,  $F_r$  and  $F_z$  are tangential, radial and axial component of body forces  $\mathbf{F} = \mathbf{j} \times \mathbf{B}$ .

Previous studies indicate that, in front of anode surface a back flow region emerges. That intensive vortexes leading to a stronger mixture of cold and hot gas. An extra cooling effect intensified by turbulence may happen in this back flow region. So that the turbulent effect is taken into account.

RNG  $K - \varepsilon$  turbulent equations:

$$\frac{1}{r} \frac{\partial}{\partial r} (r \rho v_r K) + \frac{\partial}{\partial z} (\rho v_z K) = \frac{1}{r} \frac{\partial}{\partial r} \left( r \alpha_t \mu_t \frac{\partial K}{\partial r} \right) + \frac{\partial}{\partial z} \left( \alpha_t \mu_t \frac{\partial K}{\partial z} \right) + G - \rho \varepsilon \tag{10}$$

$$\frac{1}{r} \frac{\partial}{\partial r} (r \rho v_r \varepsilon) + \frac{\partial}{\partial z} (\rho v_z \varepsilon) = \frac{1}{r} \frac{\partial}{\partial r} \left( r \alpha_\varepsilon \mu_t \frac{\partial \varepsilon}{\partial r} \right) + \frac{\partial}{\partial z} \left( \alpha_\varepsilon \mu_t \frac{\partial \varepsilon}{\partial z} \right) + \frac{\varepsilon}{k} (c_1 G - c_2 \rho \varepsilon) - R_\varepsilon \tag{11}$$

$$G = \mu_t \left\{ 2 \left[ \left( \frac{\partial v_z}{\partial z} \right)^2 + \left( \frac{\partial v_r}{\partial r} \right)^2 + \left( \frac{v_r}{r} \right)^2 \right] + \left( \frac{\partial v_z}{\partial r} + \frac{\partial v_r}{\partial z} \right)^2 + \left( \frac{\partial v_\theta}{\partial z} \right)^2 + \left( \frac{\partial v_\theta}{\partial r} - \frac{v_\theta}{r} \right)^2 \right\} \tag{12}$$

$$R_\varepsilon = \frac{c_\mu \rho \eta^3 (1 - \eta/\eta_0) \varepsilon^2}{1 + \beta \eta^3} \frac{1}{K}, \Gamma_u = \mu + \mu_t, \Gamma_T = \kappa + \frac{\mu_t C_p}{Pr_t}, \eta = S \frac{K}{\varepsilon} \tag{13}$$

$K$ ,  $\varepsilon$ ,  $S$  and  $\mu_t = \frac{\rho C_p K^2}{\varepsilon}$  are turbulent kinetic energy, turbulent dissipation rate, norm of turbulent strain rate, turbulent viscosity.  $Pr_t = 0.9$ ,  $c_\mu = 0.085$ ,  $\beta = 0.012$ ,  $\eta_0 = 4.38$ ,  $\alpha_t = 1.39$ ,  $\alpha_\varepsilon = 1.39$ ,  $c_1 = 1.42$  and  $c_2 = 1.68$  are the model constants suggested by Yakhot and Orszag [46, 47].

In energy conservation equation, we assume that the viscous dissipation and the work of the pressure gradient can be neglected due to the lower Mach number.

To unify the plasma column and the electrodes, a model presented by J. J. Lowke [4] is used. This method neglects the space-charge layer. In near-cathode region (about 0.1 mm thickness), electron number density continuity equation accounting for ambipolar diffusion is solved, and the electric conductivity is modified according to the electron number density as follow:

$$\sigma_{eff} = \frac{n_e e}{n_0 / (n_T \mu_e) + (2en_e n_{eq}) / (n_T \sigma)} \tag{14}$$

where  $n_0$  is the equilibrium neutral particle density,  $\mu_e$  is the electron mobility,  $n_T$  is the total particle density,  $n_{eq}$  is the equilibrium electron density.

The energy fluxes from plasma to cathode and anode surface are as follows:

$$F_{ca} = -\varepsilon \alpha T_c^4 - j_e \Phi_c + j_i V_i + k \frac{dT}{dn} \tag{15}$$

$$F_{an} = -\varepsilon \alpha T_c^4 + j_e \Phi_c + k \frac{dT}{dn} = 15 \tag{16}$$

$$j_R = AT_c^2 \exp \frac{-\Phi_c e}{k_B T_c} \tag{17}$$

where,  $\varepsilon$ ,  $T_c$ ,  $\alpha$ ,  $\Phi_c$ , and  $V_i$  are the emissivity of the surface, the surface temperature, the Stefan–Boltzmann constant, the work function, and the ionization potential respectively.  $j_e$ ,

$j_R$  is the electron current density and theoretical thermionic emission current density given by the Richardson equation.  $A$  is the thermionic emission constant for the surface of the cathode,  $e$  is the electronic charge,  $k_B$  is Boltzmann's constant.  $j$ , the current density at the surface of the cathode, can be obtained from the current continuity equation. At the cathode surface,  $j_i$  and  $j_e$  are set to  $j - j_R$  and  $j_R$  respectively, when  $j$  is larger than  $j_R$ . They will be set to 0 and  $j$  respectively, when  $j$  is smaller than  $j_R$ .

### Domain and Boundary Conditions

The configuration of calculation domain in this paper is the same as that in Ref. [39], which has been usually employed to investigate the arc characteristics [11, 39, 48]. The calculation domain consists of anode, cathode, near-cathode region and arc column, as shown in Fig. 2. The calculation domain is around 35 mm in radius and length, much larger than arc plasma area formed in front of cathode tip, so that the influence of inlet and outlet on the accuracy of results can be reduced to the minimum. In cathode body J–A–B–L–K–J and anode body C–D–E–F–C solid thermal conduction and electric potential equations are solved. The cathode is assumed to be made of tungsten while the anode is copper and water cooled.

The boundary conditions of the primary variables are summarized in Table 1. A–B–C–D is the axis of symmetry of the system, where the axially symmetric conditions are employed for the independent variables. I–H is the gas inlet, I–J–K–B is the plasma-cathode interface, F–C is the plasma-anode interface, F–G–H is the gas outlet. At the gas inlet, the boundary conditions for turbulent kinetic energy and its dissipation rate are taken as  $K = 0.005u_{in}^2$  and  $\varepsilon = 0.1 \rho K^2/\mu$ , which are typically used in hydraulic flow calculations. At the gas outlet,  $\frac{\partial K}{\partial n} = 0$  and  $\frac{\partial \varepsilon}{\partial n} = 0$ . At A–I, cathode bottom, current density is a given constant  $j_{in}$  and the total current is 200A.

The cathode material is cerium-tungsten. The coefficients used for cathode are listed as follows:  $A = 3 \times 10^4 \text{ A/m}^{-2}\text{K}^{-2}$ ,

$$\Phi_c = 2.63 \text{ eV},$$

$$k_{ca} = (186 - 0.0737T + 1.36 \times 10^{-5}T^2) \text{ W/m},$$

$$\sigma = \frac{10^9}{(-33.6 + 0.278T + 1.06 \times 10^{-5}T^2)} \text{ S/m}.$$

The anode material is copper, of which the thermal conductivity and electric conductivity are:

$$k_{an} = 400 \text{ W/mK},$$

$$\sigma = 5.714 \times 10^7 \text{ S/m}.$$

## Results and Discussions

Numerical results are achieved by FLUENT<sup>®</sup> with user-defined-functions developed by Li and Bai [19, 22, 23, 43]. The user-defined scalar (UDS) has been set to calculate the

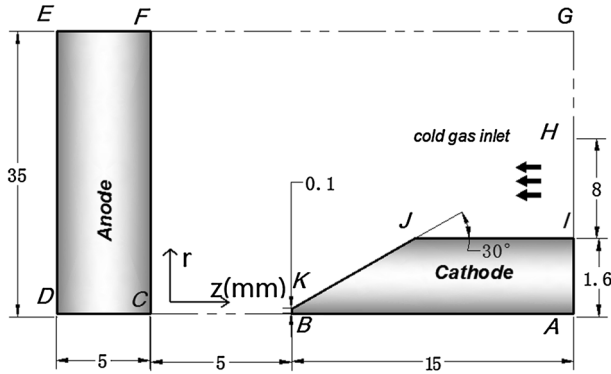


**Fig. 2** Scheme of half section of simulation domain

**Table 1** Boundary conditions

Boundary	T	P	$v$	$\varphi$	A
I–H	300 K	1 atm	0.668 m/s	$\frac{\partial \varphi}{\partial n} = 0$	$\frac{\partial A}{\partial n} = 0$
H–G–F	$\frac{\partial T}{\partial n} = 0$	$\frac{\partial P}{\partial n} = 0$	$\frac{\partial v}{\partial n} = 0$	$\frac{\partial \varphi}{\partial n} = 0$	$\frac{\partial A}{\partial n} = 0$
F–E–D	300 K	–	–	$\varphi = 0$	$\frac{\partial A}{\partial n} = 0$
I–J–K–B	Flux $F_{ca}$	–	0	Coupled	Coupled
F–C	Flux $F_{an}$	–	0	Coupled	Coupled
I–A	1,000 K	–	–	$J = j_{in}$	$\frac{\partial A}{\partial n} = 0$

electromagnetic field, and user-defined functions (UDF) have been written to implement the extra source terms and transport coefficients. In simulation, the total current of arc is 200A while the AMF is set to 0T, 0.01T, 0.015T and 0.02T, and the gap between electrodes is 5 mm. Transport coefficients are taken from the Ref. [49].

To exhibit the AMF’s effects on cathodic arc attachment, the current density profiles along cathode surface B–K–J are shown in Fig. 3. The figure shows that, the order of magnitude obtained for the current density at the cathode tip is  $1 \times 10^8$  A/m<sup>2</sup>. The peak of current density is at the tip corner K, which is resulted from the cathode geometry. Notably, as AMF increases, the current density decreases in the attachment fringe and increases at the cathode tip. That indicates, cathodic arc attachment retracts towards the cathode tip under the influence of AMF.

In Fig. 4, we present the comparison of temperature maps between results from the VCAM and the FCAM. The cathodic boundary condition (current density and temperature) for the FCAM is fixed as that predicted by the VCAM without AMF.

For the VCAM, the maximum temperature of plasma, close to the cathode tip, increases as the AMF increases. The high temperature core elongates under 0.01T AMF, and then retracts towards the cathode tip and expands radially under 0.015T/0.02T AMF. The significant discrepancies resulted from the two models are as follows: (1) The maximum temperature of plasma from VCAM increases obviously with AMF. That is in line with the trend of the experimental results [16]. However the maximum temperature from FCAM keeps almost unchanged; (2) When the AMF is set to 0.01T, the high temperature contour (for example, higher than 18,000 K) from the VCAM elongates greater than FCAM; (3)

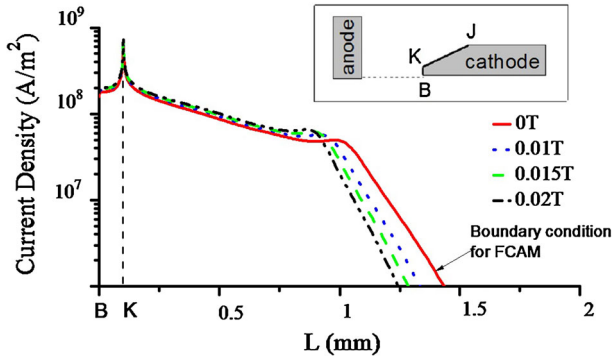


**Fig. 3** Current density profiles along line B-K-J on the cathode surface

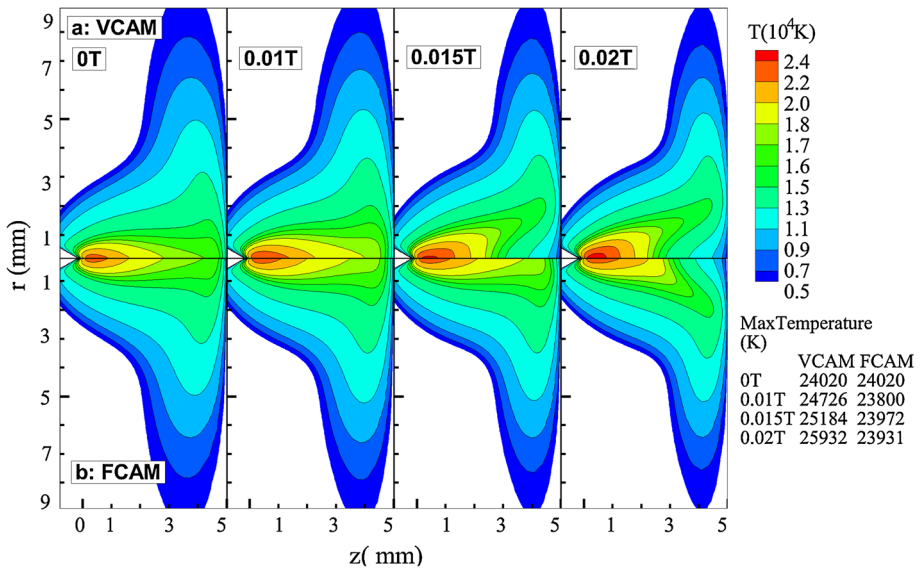


**Fig. 4** Temperature maps dependent of AMFs when using (a) VCAM; (b) FCAM

With 0.015T and 0.02T AMF, the high temperature region from the VCAM retracts towards the cathode tip and expands in the radial direction more intensively. A larger low temperature hollow forms near the anode.

The shrinkage of the cathodic arc attachment is able to increase current density in front of the cathode tip. The plasma temperature there is hence enhanced.

The plasma flow of the free arc from the cathode to the anode is resulted from the “cathode jet” [50], which is “Magneto-Hydro Dynamics (MHD) pumping effect”. The AMF induces the arc column swirling, and causes the plasma centrifugal flow, which induces a “MHD pumping effect” on the plasma. For the VCAM, the pumping effect, with the addition of an enhanced cathode jet resulted from the shrinkage of the cathodic root, prolongs the high temperature plasma core more intensively than that from the FCAM, under 0.01T AMF.



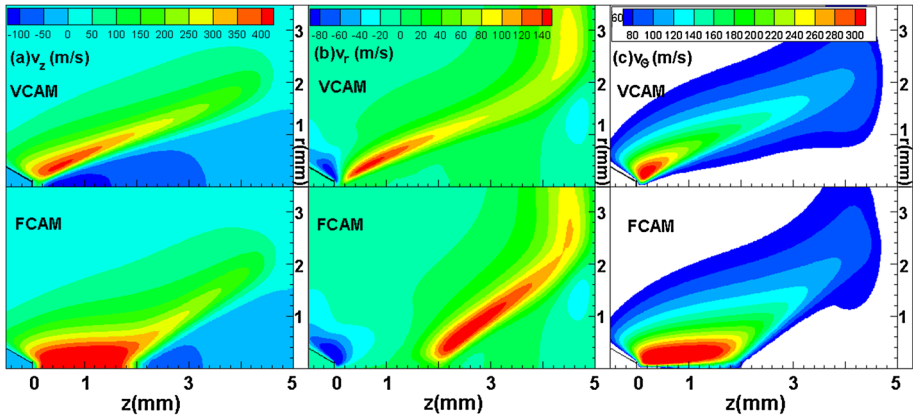


**Fig. 5** Velocity maps for AMF 0.02T

The shrinkage of the cathodic root increases the radial current density  $j_r$  near the cathode tip. Thus the swirling flow near the cathode tip would increase, since the Lorentz Force causing swirling is proportional to  $j_r \times B_z$  ( $B_z$ , AMF). The final result is, swirling flow for the VCAM is more off axis than from the FCAM. That is illustrated in Fig. 5. Starting from the cathode tip, the deviation of the maximum swirling speed ( $v_\theta$ ) from the axis from the VCAM is greater than from the FCAM on the same cross-section. That induces more centrifugal flow ( $v_r$ ) starting from the cathode tip, so as to change the upstream flow direction of the plasma for the VCAM. While the centrifugal flow from the FCAM develops far from the cathode tip. As a result, low temperature hollow around the axis for the VCAM exhibits larger than that for the FCAM, under 0.015T and 0.02T AMF.

The radial profiles of the current density along the anode interface reflect the configurations of the anodic arc attachment and of the arc column near the anode. Figure 6 shows current density profiles from two models. With 0.01T AMF, current density profile from the VCAM presents a small “concave” shape at axis, but not a concave from the FCAM, although the longer high temperature core for the VCAM. That means stronger swirling flow from the VCAM than from the FCAM under 0.01T AMF. Centrifugal flow induced by swirling flow changes the direction of the plasma flow near the cathode tip, so as to change configuration of the arc column as well as the anodic attachment. With 0.02T AMF, the concave of current density profile from VCAM exhibits much larger and deeper than those from FCAM. That is in accordance with the low temperature hollow of the arc column configuration, as shown in Fig. 4. Also, the circumjacent current density from the VCAM is slightly smaller than that from the FCAM. Those means that the arc column near the anode from the VCAM is compressed more than that from the FCAM under 0.02T.

To make a better understanding of the AMF effects from the VCAM, in Fig. 7, we show the temperature maps with streamlines for a small region near the cathode tip. The groups of flow lines in order have same origins at the gas inlet. As AMF increases, the streamlines near the cathode shift and crowd towards the axis, while the outer temperature contours (lower than 16,000 K) shift towards the cathode tip, although high temperature core (higher than 16,000 K) expands. That means the gas flow towards the area in front of the cathode tip is intensified with the AMF. That would compress and cool the arc near the cathode tip. As a result, the cathodic arc attachment retracts towards the cathode tip when using the VCAM. It does not from the FCAM, of course. It is notable that, with 0.02T AMF, the streamlines in front of the cathode tip from the FCAM are more crowded than

**Fig. 6** Comparisons of current density profiles along anode surface

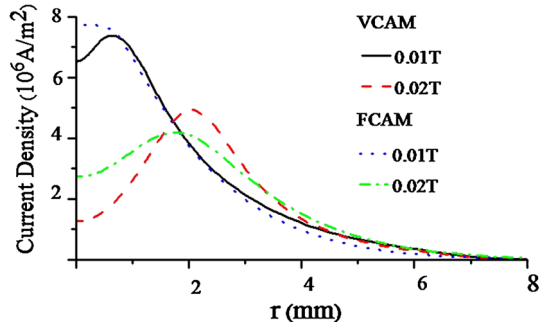
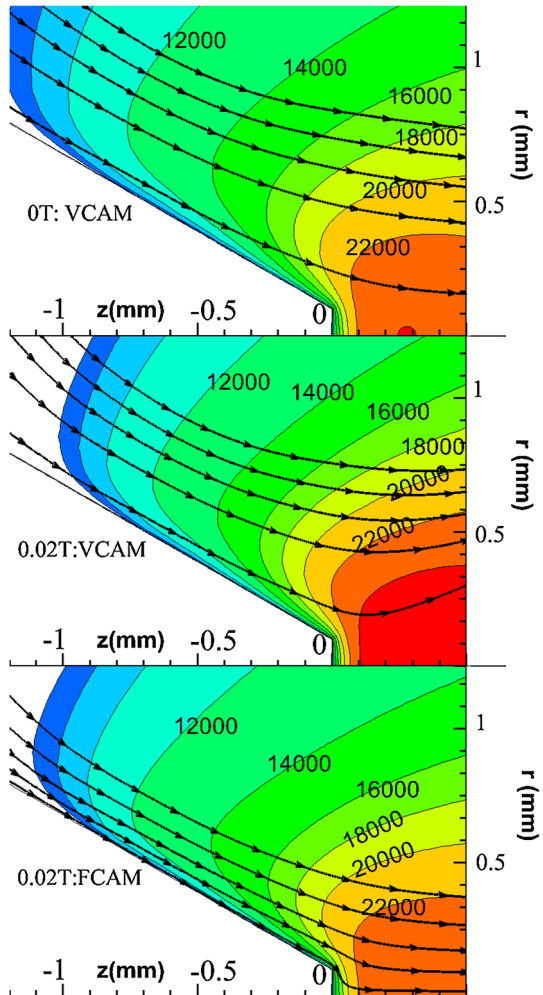


**Fig. 7** Streamlines and their shift for different AMFs from the VCAM



from the VCAM, and the streamlines from the FCAM almost parallel the axis while those from the VCAM depart the axis. That indicates that: (1) for the FCAM, without shrinking of the arc cathodic root, “MHD pumping effect” significantly enhances axial flow in front of the cathode tip; (2) for the VCAM, due to the shrinkage of the arc cathodic attachment,  $\mathbf{j}_r \times \mathbf{B}_z$  ( $\mathbf{B}_z$ , AMF) in front of the cathode tip is increased. This changes plasma flow direction. As a consequent, under 0.02T AMF, the axial flow in front of the cathode tip is not intensified, but weakened in fact. The backflow then comes close to the cathode tip.

As shown in Fig. 8, as AMF increases, the streamlines around the arc column crowd centripetally, and the streamlines near the anode crowd axially towards the anode. Those means axial flow around the arc column is intensified, and the arc plasma is compressed centripetally around the arc column and axially near the anode. When AMF increases up to 0.015T and 0.02T, the plasma flow induced by the cathode jet and “MHD pumping effect” is dragged off axis by a centrifugal flow, which is resulted from the swirling flow due to the AMF’s effecting on radial current component. Then a recirculation zone appears. And that forms a low temperature hollow around axis near the anode.

To validate the turbulence assumption, we illustrate in Fig. 9, (a) the ratio of turbulent viscosity to molecular viscosity and (b) the ratio of turbulent thermal conductivity to molecular thermal conductivity. The maximum value of the former ratio is about 2.8, locating in front of the cathode tip. The maximum value of the latter ratio is about 1.9, locating in the outer arc column. This indicates that the swirl flow induces an obvious turbulent effect. The turbulent flow assumption is valid.

The AMF has changed the configuration of the cathodic arc attachment, the arc column and the anodic arc attachment. Consequently, that should influence arc parameters (voltage, power and etc.), as well as heat transfer to anode surface. They are listed in Table 2. The arc column voltage drops from two models increase as the AMF increases. The increment of the voltage drop mainly results from the increase of the current density near

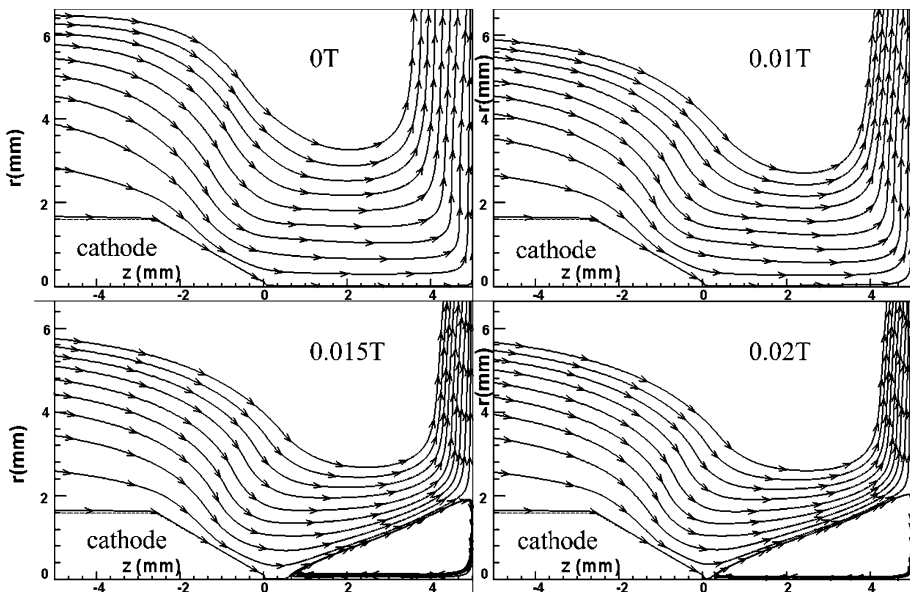
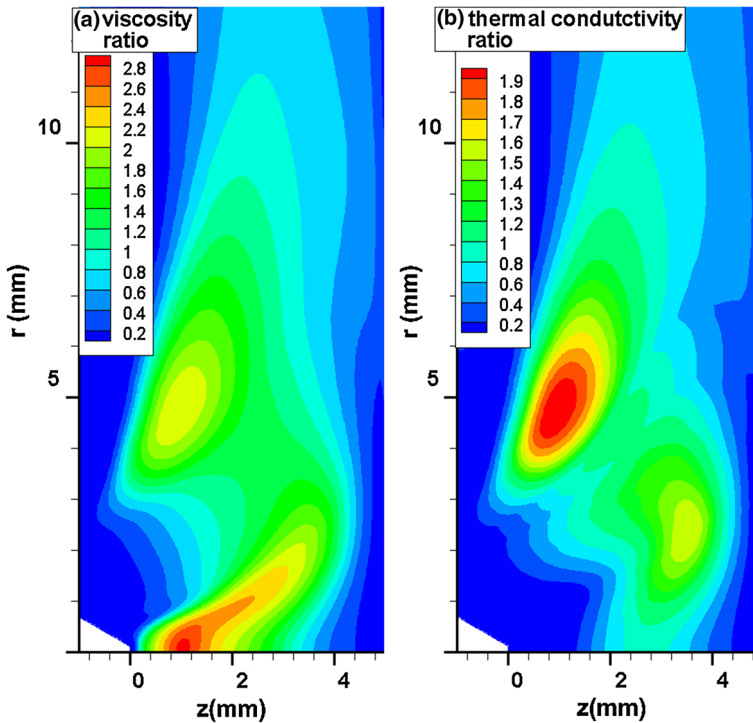


Fig. 8 Streamlines at vertical-section for different AMF



**Fig. 9** **a** The ratio of turbulent viscosity to molecular viscosity and **b** the ratio of turbulent thermal conductivity to molecular thermal conductivity: AMF, 0.02T

**Table 2** Arc column voltage drop and total/conduction heat to anode

AMF	Arc voltage		Total heat to anode		Conduction heat to anode	
	VCAM (V)	FCAM (V)	VCAM (W)	FCAM (W)	VCAM (W)	FCAM (W)
0T	9.8	9.8	2,750	2,750	1,820	1,820
0.01T	10.9	10.85	2,900	2,806	1,970	1,876
0.015T	11.28	11.18	2,975	2,853	2,045	1,923
0.02T	11.58	11.43	3,020	2,921.6	2,090	1,991.6

the cathode tip and the conduction length of the arc column. Under 0.02T AMF, the increment of the arc voltage drop from the VCAM is about 1.78 V, which is 0.15 V greater than from the FCAM. The increment of arc voltage drop would increase heating power to the arc column, so as to increase its temperature. The total heat flux to anode surface from the VCAM increases by 270 W, which is 98.4 W greater than from the FCAM.

## Conclusions

Numerical researches on AMF's effects on an arc between pointed rod cathode and plate anode are performed by using a LTE model of unifying the plasma and electrodes. The results are obtained at the condition of atmospheric pressure, 200A argon arc, 0–0.02T

AMF, and 0.668 m/s inlet gas speed. The cathode is of 3.2 mm diameter and 60° cone angle. The arc column exhibits a typical hollow-bell shaped configuration under AMF. The AMF induces arc rotating and results in a MHD pumping effect, which makes a main contribution to the shrinkage of cathodic arc attachment. The constricted cathodic arc attachment increases the current density in front of the cathode tip, so as to increase the temperature there. Also, it increases the radial current density near the cathode tip, which then changes plasma flow direction there due to the AMF. It is the variation of the cathodic arc attachment that remarkably generates the configurations of the arc column and anodic arc attachment, different from those from the FCAM. Compared with the simulation of the FCAM, one from VCAM: (1) obtains a shrinking cathodic arc attachment; (2) produces a higher plasma temperature near the cathode tip and a larger low temperature hollow near the anode; (3) the profile of current density on the anode exhibits a bigger concave; (4) predicts a higher arc column voltage drop and total heating power to anode.

**Acknowledgments** The work is supported by The National Natural Science Foundation of China: NSFC11035005, NSFC50876101.

## References

1. Fauchais P, Vardelle A (1997) Thermal plasmas. *IEEE Trans Plasma Sci* 25:1258–1280
2. Pfender E (1999) Thermal plasma technology: where do we stand and where are we going? *Plasma Chem Plasma Process* 19:1–31
3. Sansonnens L, Haidar J, Lowke JJ (2000) Prediction of properties of free burning arcs including effects of ambipolar diffusion. *J Phys D Appl Phys* 33:148–157
4. Lowke JJ, Morrow R, Haidar J (1997) A simplified unified theory of arcs and their electrodes. *J Phys D Appl Phys* 30:2033–2042
5. Haidar J (1999) Non-equilibrium modeling of transferred arcs. *J Phys D Appl Phys* 32:263–272
6. Cram LE (1983) A Model of the Cathode of a Thermionic Arc. *J Phys D Appl Phys* 16:1643–1650
7. Bini R, Monno M, Boulos MI (2006) Numerical and experimental study of transferred arcs in argon. *J Phys D Appl Phys* 39:3253–3266
8. Haidar J (1998) A theoretical model for gas metal arc welding and gas tungsten arc welding. *J Appl Phys* 84:3518–3529
9. Hsu KC, Pfender E (1983) 2-Temperature modeling of the free-burning, high-intensity arc. *J Appl Phys* 54:4359–4366
10. Baeva M, Kozakov R, Gorchakov S, Uhrlandt D (2012) Two-temperature chemically non-equilibrium modelling of transferred arcs. *Plasma Sources Sci Technol* 21:055027
11. Li HP, Benilov MS (2007) Effect of a near-cathode sheath on heat transfer in high-pressure arc plasmas. *J Phys D Appl Phys* 40:2010–2017
12. Benilov MS, Benilova LG, Li HP, Wu GQ (2012) Sheath and arc-column voltages in high-pressure arc discharges. *J Phys D Appl Phys* 45:355201
13. Goldman K, White ES (1965) The effect of an external axial magnetic field on electric arc. *Brit J Appl Phys* 16:907
14. Kang YH, Na SJ (2002) A study on the modeling of magnetic arc deflection and dynamic analysis of arc sensor—a magnetic field applied to a welding arc produced an output signal beneficial for an arc sensor. *Weld J* 81:8S–13S
15. Gold RS (1996) Arc lamp with external magnetic means. United States of America Patent 5(589):726
16. Wang Cheng CT (2014) Axial magnetic field effects on xenon short-arc lamps. *Plasma Sci Technol* (to be published)
17. Luo J, Jia CS, Wang YS, Xue J, Wu YX (2001) Mechanism of the gas tungsten-arc welding in longitudinal magnetic field controlling—I. Property of the arc. *Acta Metall Sin* 37:212–216
18. Luo J, Jia CS, Wang YS, Xue J, Wu YX (2001) Mechanism of the gas tungsten-arc welding in longitudinal magnetic field controlling—II. Model of the arc. *Acta Metall Sin* 37:217–220
19. Li LC, Xia WD (2008) Effect of an axial magnetic field on a DC argon arc. *Chinese Phys B* 17:649–654
20. Li LC, Bai B, Zhou ZP, Xia WD (2008) Axial magnetic-field effects on an argon arc between pin and plate electrodes at atmospheric pressure. *IEEE Trans Plasma Sci* 36:1078–1079

21. Yin X, Gou J, Zhang J, Sun J (2012) Numerical study of arc plasmas and weld pools for GTAW with applied axial magnetic fields. *J Phys D Appl Phys* 45:285203
22. Li LC (2008) Experimental observation and numerical analysis of D.C. arc plasmas dispersed by Magnetism. University of science and technology of China, Hefei
23. Bai B (2012) The simulation of magnetically dispersed arc plasma coupled with electrode. University of science and technology of China, Hefei
24. Li LC (2008) Experimental observation and numerical analysis of D.C. arc plasmas dispersed by magnetism. University of science and technology of China, Hefei
25. Zha J (2013) The experimental study of the magnetically rotating arc and the dispersed arc plasma. University of Science and Technology of China, Hefei
26. Gonzalez JJ, Cayla F, Freton P, Teulet P (2009) Two-dimensional self-consistent modelling of the arc/cathode interaction. *J Phys D Appl Phys* 42:145204
27. Benilov MS, Cunha MD (2002) Heating of refractory cathodes by high-pressure arc plasmas: I. *J Phys D Appl Phys* 35:1736–1750
28. Benilov MS, Marotta A (1995) A Model of the Cathode Region of Atmospheric-Pressure Arcs. *J Phys D Appl Phys* 28:1869–1882
29. Botticher R, Botticher W (2001) Numerical modelling of a dynamic mode change of arc attachment to cathodes of high-intensity discharge lamps. *J Phys D Appl Phys* 34:1110–1115
30. Botticher R, Botticher W (2000) Numerical modelling of arc attachment to cathodes of high-intensity discharge lamps. *J Phys D Appl Phys* 33:367–374
31. Coulombe S, Meunier JL (2000) Theoretical prediction of non-thermionic arc cathode erosion rate including both vaporization and melting of the surface. *Plasma Sources Sci T* 9:239–247
32. Coulombe S, Meunier JL (1997) Arc-cold cathode interactions: parametric dependence on local pressure. *Plasma Sources Sci Technol* 6:508–517
33. Benilov MS (1998) Nonlinear surface heating of a plane sample and modes of current transfer to hot arc cathodes. *Phys Rev E* 58:6480–6494
34. Bini R, Monno M, Boulos MI (2007) Effect of cathode nozzle geometry and process parameters on the energy distribution for an argon transferred arc. *Plasma Chem Plasma Process* 27:359–380
35. Menart J, Lin L (1999) Numerical study of a free-burning argon arc with copper contamination from the anode. *Plasma Chem Plasma Process* 19:153–170
36. Blais A, Proulx P, Boulos MI (2003) Three-dimensional numerical modelling of a magnetically deflected dc transferred arc in argon. *J Phys D Appl Phys* 36:488–496
37. Zhu PY, Lowke JJ, Morrow RHN (1992) A unified theory of free burning arcs, cathode sheaths and cathodes. *J Phys D Appl Phys* 25:1221–1230
38. Simonin O, Delalondre C, Viollet PL (1992) Modeling in thermal plasma and electric-arc column. *Pure Appl Chem* 64:623–628
39. Lowke JJ, Kovitya P, Schmidt HP (1992) Theory of free-burning arc columns including the influence of the cathode. *J Phys D Appl Phys* 25:1600–1606
40. Zaehr J, Fuessel U, Hertel M, Lohse M, Sende M, Schnick M (2012) Numerical and experimental studies of the influence of process gases in TIC welding. *Weld World* 56:85–92
41. Schnick M, Dreher M, Zschetsche J, Fuessel U, Spille-Kohoff A (2012) Visualization and optimization of shielding gas flows in arc welding. *Weld World* 56:54–61
42. Schnick M, Fussel U, Spille-Kohoff A (2010) Numerical investigations of the influence of design parameters, gas composition and electric current in plasma arc welding (Paw). *Weld World* 54:R87–R96
43. Bai B, Zha J, Zhang XM, Wang C, Xia WD (2012) Simulation of magnetically dispersed arc plasma. *Plasma Sci Technol* 14:118–121
44. Pfender E (1980) Energy-transport in thermal plasmas. *Pure Appl Chem* 52:1773–1800
45. Xia WD, Li LC, Zhao YH, Ma Q, Du BH, Chen Q, Cheng L (2006) Dynamics of large-scale magnetically rotating arc plasmas. *Appl Phys Lett* 88:211501
46. Yakhot V, Orszag SA (1986) Renormalization-Group Analysis of Turbulence. *Phys Rev Lett* 57:1722–1724
47. Yakhot V, Orszag SA, Thangam S, Gatski TB, Speziale CG (1992) Development of turbulence models for shear flows by a double expansion technique. *Phys Fluids a-Fluid* 4:1510–1520
48. Hsu KC, Etemadi K, Pfender E (1983) Study of the free-burning high-intensity argon arc. *J Appl Phys* 54:1293–1301
49. Murphy AB, Arundell CJ (1994) Transport-coefficients of argon, nitrogen, oxygen, argon–nitrogen, and argon–oxygen plasmas. *Plasma Chem Plasma Process* 14:451–490
50. Gleizes A, Gonzalez JJ, Freton P (2005) Thermal plasma modelling. *J Phys D Appl Phys* 38:R153–R183